ROYAL SOCIETY OF CHEMISTRY

PAPER

Check for updates

Metal-modified C_3N_1 monolayer sensors for battery instability monitoring†

Mingyang Gu,[a] Lin Tao, [ID] *[a] Davoud Dastan,[b] Jie Dang, [ID] [c] Timing Fang [ID] [d] and Baigang An*[a]

The pressing need for affordable gas sensors with enhanced sensitivity and selectivity in identifying hazardous gases released after the battery becomes unstable cannot be overstated. In this study, a C_3N_1 monolayer modified with Cu and Ag atoms ($Cu/Ag-C_2N_1$) was selected to achieve selective adsorption of NO_2 under the coexistence of multiple gases (PF_5, NH_3, H_2O, C_2H_4, and C_2H_6) based on density functional theory. The results demonstrate that securely anchoring metal atoms to the monolayer, as indicated by cohesion energy and *ab initio* molecular dynamics simulations, concurrently enhances the material's conductivity. Analyses of electrostatic potential and work function identified high activity sites and electron-releasing capabilities. Furthermore, the gas–solid interface structures of multiple gases on the $Cu/Ag-C_2N_1$ monolayers are revealed by the adsorption energy and distance. Importantly, NO_2 exhibits stronger adsorption energy on $Cu/Ag-C_2N_1$, reaching −3.54 and −3.27 eV, respectively. Crystal Orbital Hamilton Population and d-band center theory unveiled differences in adsorption energy resulting from the modification involving the two metals. Fascinatingly, density of states calculation demonstrates, for the first time, that the two doped metal monolayers generate a distinct response solely to NO_2 in a multi-gas coexistence setting, effectively excluding interference from water. In practice, based on Gibbs free energy and Einstein diffusion law calculations, $Cu-C_2N_1$ exhibits superior hydrophobicity, a broader temperature range and a lower diffusion activation energy barrier (2.5 kJ mol^{-1}). Our theoretical calculations demonstrate Cu's efficacy in substituting expensive Ag, yielding cost-effectiveness without compromising selectivity, response, stability, and versatility.

1 Introduction

Widespread in portable electronics and integral to the surge in electric vehicles, batteries play a pivotal role, significantly impacting the tapestry of modern society.[1–3] However, the pursuit of high-energy-density batteries raises safety concerns due to increased gas evolution, particularly with lithium metal.[4,5] Safety monitoring is vital as battery defects can trigger severe risks like electrolyte-induced heat leading to fire and explosion. This thermal runaway results in the release of harmful gases.[6] Lithium metal poses challenges due to its reactivity, potentially causing dendritic formation and a hot mixture release, a precursor to fire or explosion. Early detection of gases like NO_2, PF_5, NH_3, C_2H_4, H_2O, and C_2H_6 before thermal runaway is imperative to prevent safety hazards in practical applications.[7,8]

In recent years, an abundance of theoretical studies has delved into the design and fabrication of monolayers for detecting toxic gases. Theoretical calculations, employing density functional theory (DFT), have played a pivotal role in accurately predicting the sensing efficiency of two-dimensional (2D) monolayers and elucidating their micro-sensing mechanisms.[9–17] For instance, Sun *et al.*[18] utilized DFT calculations to analyze the adsorption behavior of six gases on an indium nitride monolayer, demonstrating its potential in detecting SO_2 and NO_2 molecules. Additionally, first-principles calculations were employed to explore the structural and electronic properties of group III nitrides and phosphides in gas adsorption. It was concluded that significant potential exists for the detection of CO_2 by these sensors. Furthermore, the introduction of transition metal doping can enhance the sensing capabilities of 2D monolayers.[19–21]

In gas-sensitive applications, 2D monolayers demonstrate exceptional performance owing to their high specific monolayer area, thermal conductivity, unique optoelectronic properties, and catalytic activity.[22–25] As chemical gas sensors, these

[a]School of Chemical Engineering, University of Science and Technology Liaoning, Anshan 114051, China. E-mail: taolin@ustl.edu.cn; bgan@ustl.edu.cn

[b]Department of Materials Science and Engineering, Cornell University, Ithaca, New York 14850, USA

[c]College of Materials Science and Engineering, Chongqing University, Chongqing 400044, China

[d]School of Chemistry and Chemical Engineering, Qingdao University, Qingdao 266071, China

monolayer offer abundance, cost-effectiveness, and easy manufacturability, and play a pivotal role in sensor technology. Among numerous 2D material-based gas sensors, their sensitivity to various toxic and explosive gases stems from gas-induced resistance changes,[26] finding wide application across diverse fields. Graphene and C_3N monolayer films, among others, have theoretically shown promising gas-sensing characteristics.[27–29] Despite this, inherent defects limit the full application potential of 2D monolayers in sensing technologies. Hence, exploring and discovering novel types of two-dimensional monolayers for gas detection become imperative to address these limitations and expand the sensor monolayer repertoire.

Creating new gas sensors to detect typical electrolyte decomposition products under harsh conditions is crucial. 2D monolayers stand out as prime candidates for such sensing applications, operating within a high temperature range and exhibiting the highest response levels.[30] Enhancing gas sensor characteristics involves monolayer material modification. Semiconductor-based metal oxide gas sensors also require temperature resistance during thermal runaway, making safety-based detectors particularly promising. These devices offer stability under high humidity conditions but demand high-temperature resilience during thermal runaway.[31,32] Metal-doped 2D material gas sensors exhibit notably high responses, showcasing how metals create a platform to merge diverse physical and chemical properties within a system. Past research has amalgamated experiments and intricate computational analyses to validate the applicability of metal-doped structures in sensor applications.[33–36] These studies have visualized the gas sensing traits, portraying the adsorption performance of gas sensors for practical implementation.

However, the electrical response of the sensing monolayer originates from the cumulative effect of each gas. The significant scientific challenge lies in the absence of an effective method to systematically allocate the contribution of each gas. Consequently, in the case of the simultaneous adsorption of multiple gases, the strategy to enhance selectivity involves eliminating the electrical response to other interfering gases, focusing solely on one specific gas.

In this study, DFT was employed to calculate the response of $Cu/Ag–C_2N_1$ in the presence of multiple gases (PF_5, NO_2, NH_3, H_2O, C_2H_4, and C_2H_6). Initially, 2D monolayers doped with these two metals were constructed, and their stability and plausibility were examined from various perspectives. Subsequently, the adsorption behavior of multiple gases on the doped monolayer was comprehensively calculated, elucidating differences in adsorption performance based on methods such as d-band center theory and Crystal Orbital Hamiltonian Population (COHP). Utilizing the density of states (DOS) method, the electrical signal response behavior of the monolayer during the adsorption of multiple gases for selective adsorption was evaluated. Finally, the practical applicability of the sensors was explored by computing the Gibbs free energy of gas adsorption and the recovery time of the electrical signal. Our theoretical exploration offers novel insights for designing highly selective gas sensors in battery instability monitoring.

2 Results and discussion

2.1 Structural characterization

The optimized structures of the $Cu/Ag–C_2N_1$ monolayer and six gas molecules (PF_5, NO_2, NH_3, H_2O, C_2H_4, and C_2H_6) are shown in Fig. 1a. It exhibits a top-down view of the metal-modified C_2N_1 monolayer, comprising a pattern of corner rings formed by C–N–C–C sequences, while also illustrating the interaction sites of Ag and Cu. In detail, the P–F bond length in PF_5 is 1.58 Å, the N–O bond length in NO_2 is 1.27 Å, the N–H bond length in NH_3 is 1.03 Å, and the H–O bond length in H_2O is 0.98 Å. For C_2H_4, the C–H bond length is 1.09 Å, and the C–C bond length is 1.33 Å. For C_2H_6, the C–H bond length is 1.06 Å, and the C–C bond length is 1.53 Å. These data calculated in this work are consistent with those previously reported,[37–44] demonstrating that the selected calculation parameters are reasonable and accurate. Fig. 1b and c depict the main view of the monolayer of $Ag–C_2N_1$ and $Cu–C_2N_1$, respectively. Clearly, both doped metals are situated atop the 2D material, creating the most stable structure, in accordance with earlier research observations.[28] So as to understand the monolayer stability of doped metal atoms from the point of view of charge density, Fig. 1b and c also illustrate distinct charge density distribution. The noticeable increase in red indicates a heightened charge density of electronic wavefunction, predominantly around the C and N atoms, confirming its high charge acceptance. Both Ag and Cu act as electron donors, transferring electrons to C_2N_1. Therefore, to maintain an optimal stable structure, the doped metal atoms ultimately position themselves above the monolayer, resulting in substrate deformation.

Additionally, cohesion energy (E_{coh}) analyses were conducted to quantitatively explore the anchoring of metal atoms onto the monolayer. First, the E_{coh} was analyzed as:[45]

$$E_{coh} = \frac{(n_1 E_{TM} + n_2 E_C + n_3 E_N - E_{C_2N_1})}{(n_1 + n_2 + n_3)} \tag{1}$$

where E_C and E_N represent the energies (eV) of C and N atoms, respectively. n_1, n_2, and n_3 are the numbers of metal, C, and N atoms. The E_{coh} of the initial C_3N_1 monolayer was calculated to be 7.01 eV. After metal doping, it decreased to 6.67 eV for $Cu–C_2N_1$ and 6.70 eV for $Ag–C_2N_1$, showcasing a reduction within the expected range of 4%. This highlights the stable bonding of metals to the monolayer without undergoing aggregation. To evaluate the dynamic stability of this structure, *ab initio* molecular dynamics simulation was conducted. A total of 5000 steps were calculated over 50 ps, using a time step of 10 fs for output. The results, confirming the stability of the monolayer structures, are illustrated in Fig. S1.† In the realm of top-notch gas sensors, it's crucial to understand the electron transport capabilities and active sites of the material for optimal performance. The electrostatic potential and work function were calculated, with the work function representing the minimum energy required to remove electrons from the monolayer. As shown in Fig. S2,† the results reveal a comparable work function for $Ag–C_2N_1$ (3.67 eV) and $Cu–C_2N_1$ (3.72 eV), suggesting a similar electron migration capability. Furthermore, based on
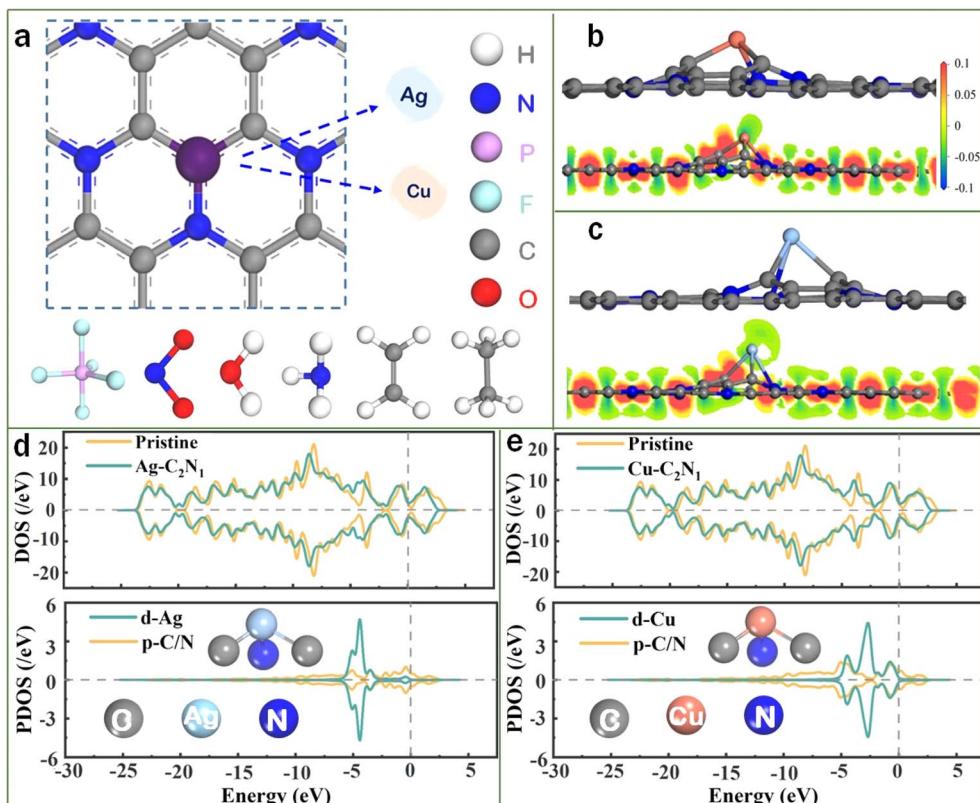
Fig. 1 (a) Structures of the Cu/Ag–C_2N_1 monolayer, PF_5, NO_2, NH_3, H_2O, C_2H_4, and C_2H_6. (b and c) Stable structure and charge density distribution of (b) Cu–C_2N_1 and (c) Ag–C_2N_1. (d and e) DOS and PDOS of (d) Ag–C_2N_1 and (e) Cu–C_2N_1. Densities are displayed with an isosurface and the interval of isovalues is between −0.1 and 0.1 e Å^{-3}.

the high electrostatic potential, it can be confirmed that the doped metal sites exhibit heightened activity.

Based on previous research,[12,19,46–49] the height of the DOS curve at the Fermi level can reflect the quality of material conductivity. In other words, higher peaks indicate better conductivity. Conductivity stands as a crucial criterion for high-performance gas sensors. Therefore, this study employs this approach to assess the impact of introducing doping metals on the material's conductivity. In Fig. 1d and e, the overall DOS demonstrates a slight increase in the curve around the Fermi level after the introduction of doping metals, indicating an enhancement in the material's conductivity. Additionally, partial density of states (PDOS) calculations were conducted to delve deeper into the behavior of the doped metal atoms. Fig. 1d and e display the d orbitals of the metal atoms and the p-orbitals of nonmetallic C/N in the monolayer. Typically, transition metal d-orbitals play a significant role in bonding. The outcomes reveal a noticeable alignment between the d orbital of Ag and the p orbital of C/N within the material. Furthermore, the hybridization of Cu's d orbital with C/N's p orbital is more prominent and situated at a higher energy level. The findings indicate that Cu and Ag can be securely affixed to the C_2N_1 monolayer. This indicates a robust interaction between the doped metal atoms and the monolayers, ensuring structural stability.

2.2 Gas sensing performance

2.2.1 Gas adsorption behavior. In this section, the optimal gas adsorption configurations were initially identified. Subsequently, the adsorption energy and distance were quantitatively analyzed. Finally, the differences in gas adsorption performance were elucidated using COHP and d-band center theory. As depicted in Fig. S3–S14,† various gas adsorption sites and configurations were explored on Ag–C_2N_1 and Cu–C_2N_1. Initially, all gas molecules positioned 2.5 Å above the monolayer underwent structural optimization calculations to determine their equilibrium positions. Based on the positive correlation between the adsorption distance and energy,[50,51] the initial configurations following this criterion were selected, as illustrated in Fig. S15 and S16.† Fig. 2 and 3 show the most stable adsorption configurations and charge densities of Ag–C_2N_1 and Cu–C_2N_1 for the six gases (C_2H_4, PF_5, C_2H_6, H_2O, NH_3, and NO_2).

In Fig. 2, the shortest atomic distances observed are 2.3 Å for Ag–C_2N_1–C_2H_4, 2.5 Å for Ag–C_2N_1–PF_5, 2.2 Å for Ag–C_2N_1–C_2H_6, 2.5 Å for Ag–C_2N_1–H_2O, 2.3 Å for Ag–C_2N_1–NH_3, and 2.2 Å for Ag–C_2N_1–NO_2. In Fig. 3, the shortest atomic distances are 2.1 Å for Cu–C_2N_1–C_2H_4, 2.5 Å for Cu–C_2N_1–PF_5, 2.0 Å for Cu–C_2N_1–C_2H_6, 2.1 Å for Cu–C_2N_1–H_2O, 2.1 Å for Cu–C_2N_1–NH_3, and 1.9 Å for Cu–C_2N_1–NO_2. After optimization, the positions of all gas molecules have shifted. The shortest distance of each gas molecule in the Ag–C_2N_1 system is slightly longer than that of
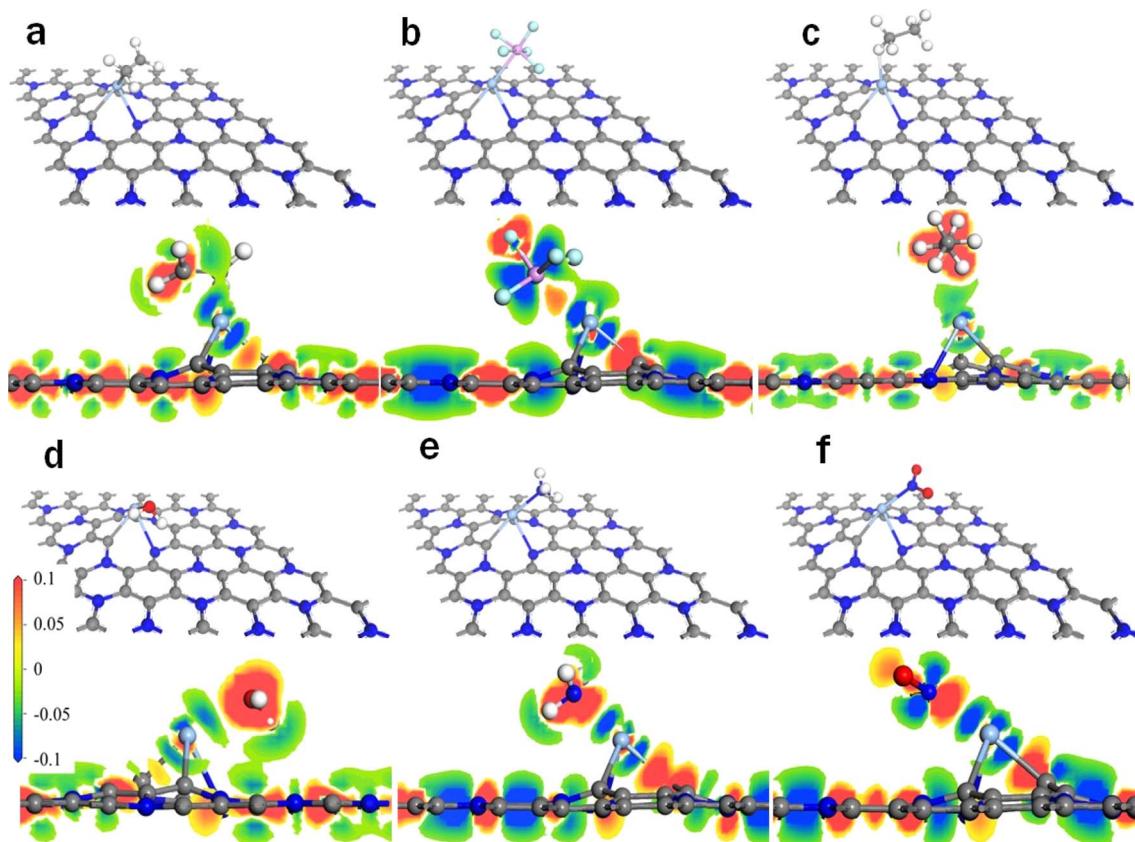
Fig. 2 Stable configurations and charge density of gas adsorbed on the Ag–C_2N_1 monolayer: (a) Ag–C_2N_1–C_2H_4, (b) Ag–C_2N_1–C_2H_6, (c) Ag–C_2N_1–PF_5, (d) Ag–C_2N_1–H_2O, (e) Ag–C_2N_1–NH_3, and (f) Ag–C_2N_1–NO_2. Densities are displayed with an isosurface and the interval of isovalues is between -0.1 and 0.1 e $Å^{-3}$.

the Cu–C_2N_1 system. Additionally, for a more visual examination of the charge accumulation and depletion during gas interaction with Cu/Ag–C_2N_1, Fig. 2 and 3 present the results of charge density analysis. The charge densities of electronic wavefunction illustrate that both Ag–C_2N_1 and Cu–C_2N_1 transfer a significant amount of charge during gas adsorption. The distinct dark red color observed around the gas molecules (C_2H_4, C_2H_6, PF_5, H_2O, NH_3, and NO_2) clearly indicates the acquisition of electrons from Ag–C_2N_1 and Cu–C_2N_1 by the gas molecules, demonstrating a strong interaction between the gas and Cu/Ag–C_2N_1. For specific charge transfer values, refer to Table S1.† The results indicate that among the six gases considered, NO_2 exhibited the most significant charge transfer to Cu/Ag–C_2N_1, suggesting its superior adsorption effect on it, particularly on the Cu–C_2N_1 monolayer.

For a more comprehensive understanding of gas adsorption behavior and to quantitatively assess the interaction forces between gases and Cu/Ag–C_2N_1, it becomes imperative to compare adsorption distances and energies. Fig. 4a and b show respectively the adsorption distance and adsorption energy. The adsorption energy is defined as:[52–54]

$$E_{ads} = E_{total} - (E_{monolayer} + E_{gas}) \qquad (2)$$

where E_{ads} is the adsorption energy (eV), E_{total} is the total energy of the monolayer with the gas molecule (eV), $E_{monolayer}$ is the total energy of the monolayer (eV), and E_{gas} is the total energy of an isolated gas molecule (eV). For the adsorption distance, the darker the color, the shorter the adsorption distance. From Fig. 4a it can be intuitively seen that the color of the row where Cu is located is darker than the color of the row where Ag is located, that is, the adsorption distance of the gas under the Cu system is less than that of the Ag system, indicating that the Cu–C_2N_1 monolayer has better adsorption performance for the gas. The adsorption distance of Cu–C_2N_1–NO_2 is the smallest, showcasing the exceptional adsorption effectiveness of Cu–C_2N_1 for NO_2. Additionally, Cu–C_2N_1 exhibits relatively small adsorption distances for C_2H_4, C_2H_6, NH_3, and H_2O, indicating noteworthy adsorption performance. However, the analysis of adsorption energy suggests that Cu–C_2N_1 interacts with C_2H_4, C_2H_6, and NH_3 through physical adsorption based on our previous work.[19] The column where NO_2 is situated appears significantly darker compared to the columns of the other gases (C_2H_4, C_2H_6, NH_3, H_2O, and PF_5) in Fig. 4b. This implies that among the six gases, only NO_2 exhibits a pronounced adsorption effect on the C_2N_1 monolayer after metal doping, and its adsorption energy is much stronger than that of the other five gases. This realization enables the selective adsorption of NO_2 gas on the monolayer in various gas environments, unaffected

This journal is © The Royal Society of Chemistry 2024

J. Mater. Chem. A, 2024, **12**, 15254–15264 | **15257**
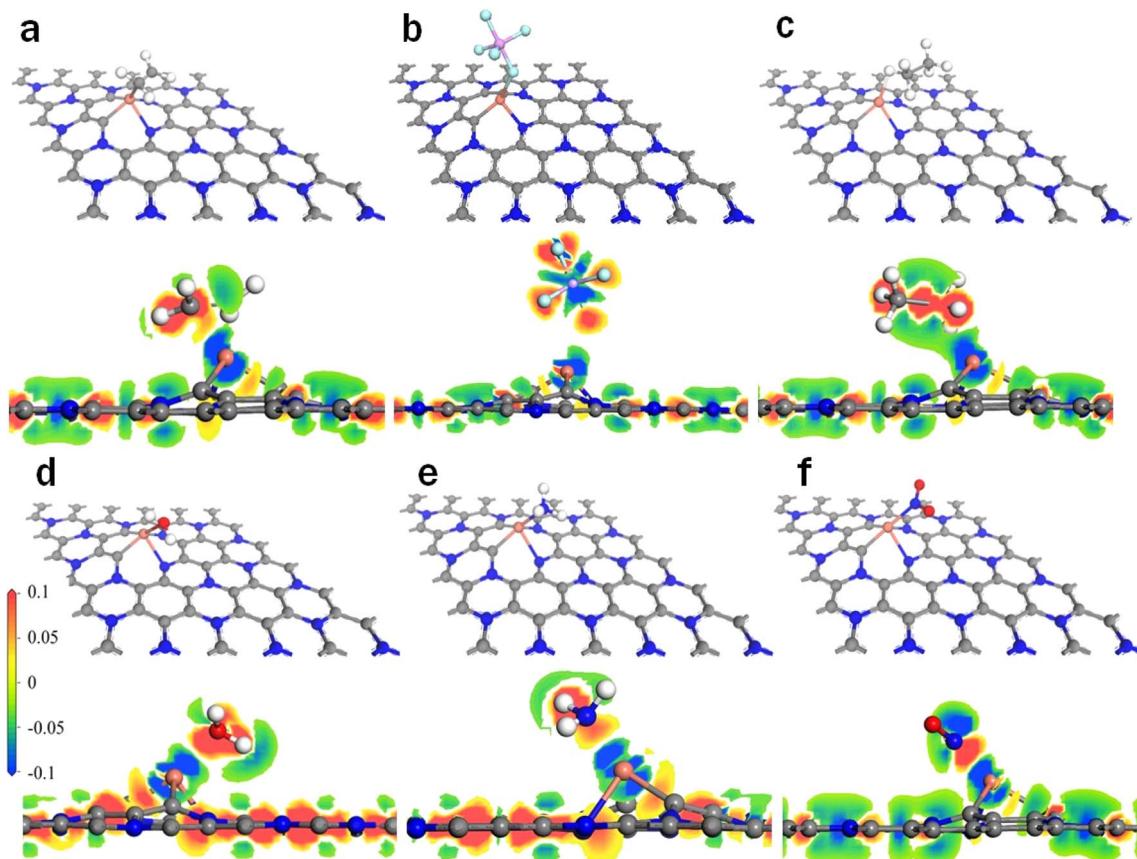
Fig. 3 Stable configurations and charge density of gas adsorbed on the Cu−C_2N_1 monolayer: (a) Cu−C_2N_1−C_2H_4, (b) Cu−C_2N_1−C_2H_6, (c) Cu−C_2N_1−PF_5, (d) Cu−C_2N_1−H_2O, (e) Cu−C_2N_1−NH_3, and (f) Cu−C_2N_1−NO_2.
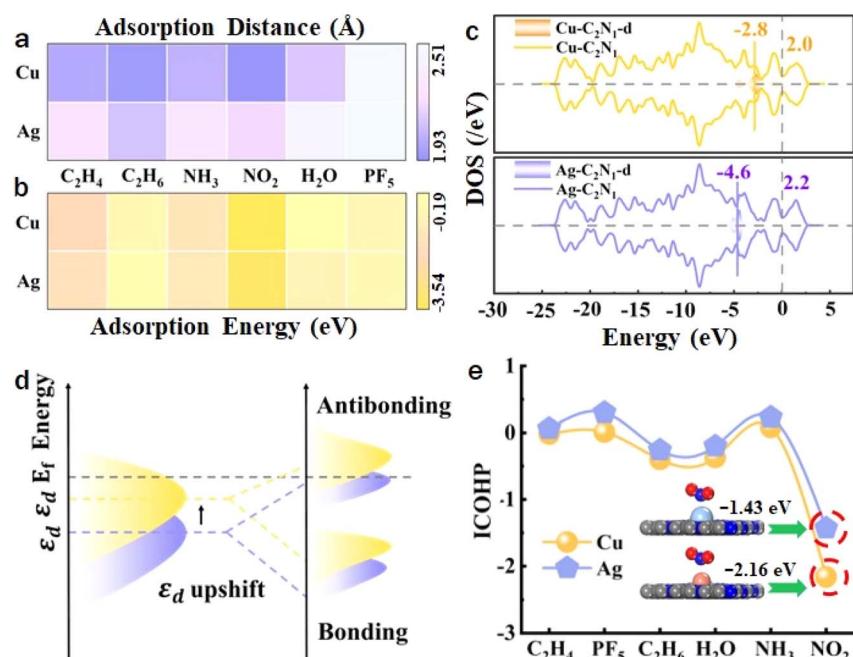
Fig. 4 (a) The adsorption distance and (b) adsorption energy of gases (C_2H_4, C_2H_6, NH_3, NO_2, H_2O, and PF_5) on the Ag−C_2N_1 and Cu−C_2N_1 monolayers. (c) The d-band center of C_2N_1 doped with metals (Cu and Ag). (d) Metal−adsorbate interaction by altering the metal d-band center. (e) ICOHP of gases on the Ag−C_2N_1 and Cu−C_2N_1 monolayers.

by the presence of other gases. Additionally, it's noteworthy that the adsorption energy of H_2O on $Cu-C_2N_1$ is weaker, indicating that $Cu-C_2N_1$ exhibits virtually no adsorption effect on H_2O. Consequently, humid environments do not affect the performance of $Cu-C_2N_1$.

Combining the different gas adsorption properties caused by the above two doped metal atoms, it can be found that the performance of Cu is better than that of Ag. For example, the adsorption energy of $Cu-C_2N_1-NO_2$ is -3.53 eV, which is stronger than that of $Ag-C_2N_1-NO_2$ (-3.26 eV). Given that d-band center theory is a useful tool for elucidating the interaction between transition metals and gas molecules, the calculation of the d-band center (ε_d) becomes imperative to unveil the underlying mechanism. The ε_d can be calculated as:[55–57]

$$\varepsilon_b = \frac{\int_{-\infty}^{\infty} n_d(\varepsilon)\varepsilon \ d\varepsilon}{\int_{-\infty}^{\infty} n_d(\varepsilon) \ d\varepsilon} \tag{3}$$

where ε is the energy and $n_d(\varepsilon)$ is the density. Fig. 4c shows the ε_d of $Cu/Ag-C_2N_1$. The larger the ε_d (close to the Fermi level), the better the adsorption effect on gas. It is better proved that NO_2 has the greatest adsorption strength on $Cu-C_2N_1$. Fig. 4d shows that the ε_d of $Cu-C_2N_1$ is closest to the Fermi level, demonstrating that the proportion of unoccupied antibonding states increases, resulting in the strongest interaction between NO_2 and $Cu-C_2N_1$.

To expose disparities in gas adsorption energy on $Cu-C_2N_1$ and $Ag-C_2N_1$ from a chemical bonding perspective, the chemical bond is categorized into bonding and anti-bonding, with bonding playing the decisive role. COHP analysis is employed for a more accurate examination of interatomic forces during gas adsorption.[58–61] The detailed calculation results are displayed in Fig. S17 and S18.† COHP represents the respective contributions of bonding and antibonding and shows the strength of the chemical bond between atoms, and the larger the bonding state below the Fermi level, the smaller the antibonding state, the stronger the bonding ability between the two atoms. In the example Fig. S17† of $Ag-C_2N_1-PF_5$, there are a large number of anti-bonds below the Fermi level, resulting in a huge internal stress between Ag and F atoms, and the anti-bonds in the system cause repulsion between the atoms, and the interaction cannot be stable. In contrast, there is a large amount of bonding below the Fermi level in $Cu-C_2N_1-NO_2$ in Fig. S18,† indicating that there is a strong force between Cu and N, which confirms the strong interaction between $Cu-C_2N_1$ and NO_2. A more quantitative explanation can be provided by calculating the integral COHP (ICOHP) value obtained by calculating the energy integral from negative infinity to the Fermi level. The more negative the ICOHP value, the stronger the interaction between metal atoms and gas atoms, as shown in Fig. 4e. Compared to the other five gases, NO_2 exhibits the most prominent ICOHP values on $Cu-C_2N_1$ and $Ag-C_2N_1$. Therefore, this result substantiates the clear advantage of competitive adsorption for NO_2 on $Cu-C_2N_1$.

2.2.2 Electrical response behavior. The selectivity is the most crucial performance indicator for gas sensors. Based on our previous work,[19,47,48] the DOS at the Fermi level can effectively represent the material's conductivity. Therefore, the electrical response behavior induced by the adsorption of various gases on the $Cu/Ag-C_2N_1$ monolayer is comprehensively analyzed. Detailed calculation results are presented in Fig. S19 and S20.† To visually determine which material exhibits the best selective performance, all electrical response values are optimized to obtain the selectivity index shown in Fig. 5. This selectivity is derived from the comparison of the electrical conductivity before and after gas adsorption. If the conductivity remains unchanged, it indicates that the gas has no effect on the material. Conversely, any change suggests that the material demonstrates a sensitive response to the gas.

In Fig. 5, the conductivity of NO_2 adsorption was significantly higher than that of the background, leading to a higher electron count near this level, ultimately enhancing conductivity. In the context of NO_2 adsorption, the redistribution of charges is the primary driver behind this shift, causing a significant alteration in conductivity. The C_2N_1 monolayer modified with metal atoms (Ag and Cu) displays a selective response to NO_2 gas amidst various other gases (C_2H_4, C_2H_6, PF_5, H_2O, and NH_3). Notably, the DOS for all orbitals on the right side of the $Cu-C_2N_1-NO_2$ Fermi level surpasses that of $Ag-C_2N_1-NO_2$, indicating a more robust response of $Cu-C_2N_1$ to NO_2 compared to its $Ag-C_2N_1$ counterpart.

The discernible charge transfer path is directly reflected in the DOS alteration seen in Fig. S19 and S20.† The conductivity of C_2H_4, C_2H_6, H_2O, and NH_3 on the monolayer of $Ag-C_2N_1$ changed little after adsorption, and the conductivity decreased slightly after PF_5 adsorption. The conductivity of C_2H_6, PF_5, H_2O and NH_3 on the monolayer of $Cu-C_2N_1$ did not change significantly after adsorption, but the conductivity of C_2H_4 decreased slightly. There was no significant change in the conductivity of the gas after adsorption, which was consistent with the observed trend. Observing the changes of the DOS before and after adsorption of H_2O in Fig. S19 and S20d,† it can be found that the DOS curves before and after adsorption change very small, and there is no change at the Fermi level, which indicates that $Ag-C_2N_1$ and $Cu-C_2N_1$ have no electrical signal response to H_2O and the monolayer is hydrophobic. Interestingly, when NO_2 is adsorbed on the monolayer of $Ag-C_2N_1$ and $Cu-C_2N_1$, the $Cu/Ag-C_2N_1$ monolayer conductivity increases significantly, which is reflected in the obvious rise and left shift of the DOS curve at the Fermi level after NO_2 adsorption in the DOS diagram. This is in contrast to the DOS changes after adsorption
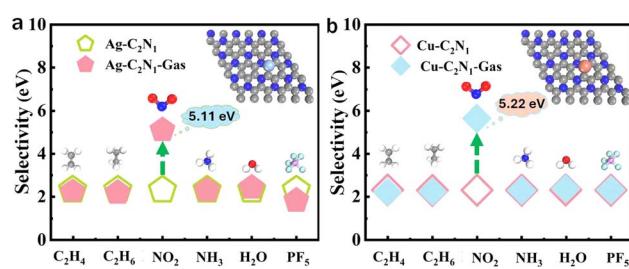

Fig. 5 Selectivity of gases on the (a) $Ag-C_2N_1$ and (b) $Cu-C_2N_1$ monolayers.

This journal is © The Royal Society of Chemistry 2024

J. Mater. Chem. A, 2024, **12**, 15254–15264 | **15259**

View Article Online

Journal of Materials Chemistry A — Paper

of other gases. It is proved that the monolayers of $Ag–C_2N_1$ and $Cu–C_2N_1$ can generate a selective electrical signal response to NO_2 gas. It is worth noting that the DOS change of NO_2 on the monolayer of $Cu–C_2N_1$ is more obvious than that of $Ag–C_2N_1$, which proves that $Cu–C_2N_1$ has a stronger effect on NO_2 and has a better effect.

In order to explore the reason why $Cu/Ag–C_2N_1$ can respond selectively to NO_2 but not to the other five gases, the adsorption mechanism was explored by PDOS. The PDOS distribution analysis showed that the more overlapping peaks in different orbitals, the stronger the hybridization between the orbitals, as shown in Fig. S19 and S20.† The conspicuous overlap observed between the metal (Ag and Cu) d-orbitals and N p-orbitals substantiates strong chemical interactions between NO_2 and $Ag–C_2N_1$, as well as $Cu–C_2N_1$. Conversely, for the remaining five gases (C_2H_4, C_2H_6, PF_5, H_2O, and NH_3), which exhibit weak adsorption on $Ag–C_2N_1$ and $Cu–C_2N_1$, their PDOS plots indicate limited interactions. In addition, the interaction between NO_2 and $Ag–C_2N_1$ is weak, evident from the small overlapping region between Ag-d and N-p orbitals. However, during the adsorption of NO_2, the hybridization between the p orbital of the N atom and the d orbital of the Cu atom is significantly enhanced, resulting in a significant increase of the PDOS of the d orbital of the Cu atom at the Fermi level, which ultimately affects the overall electrical response of the material. In summary, compared with $Ag–C_2N_1$, $Cu–C_2N_1$ has the most obvious response to NO_2 selective electrical signals and has the best effect.

Notably, the conductivity of H_2O adsorbed on the $Cu/Ag–C_2N_1$ monolayer changes very little, as depicted in Fig. 5, and no discernible changes were observed. In Fig. S19 and S20,† the overlap between the metal (Ag and Cu) d orbital and the O p orbital is still small. This observation supports the conclusion that NO_2 can be selectively detected by $Ag–C_2N_1$ and $Cu–C_2N_1$, affirming that humidity does not impede the selective electrical signal response of the doped monolayer to NO_2 in multifarious gas environments.

2.3 Applications of gas sensors

In this section, firstly, based on the detailed discussion of high sensitivity and selectivity to NO_2, the gas sensor is shown in actual usage scenarios, while also showcasing the high humidity resistance of the $Cu–C_2N_1$ monolayer. Subsequently, as a response to the various hazardous gases generated after the battery becomes thermally unstable, it is imperative to conduct a thorough assessment of the operational environment to determine the temperature tolerance of high-performance sensors. Furthermore, the gas diffusion performance of gas-sensitive materials, which determines their responsiveness, is evaluated comprehensively through molecular dynamics simulations to assess the diffusion behavior of the six gases. Finally, the desorption time of the detected gases from the gas-sensitive material is analyzed.

In Fig. 6a, the practicality of $Cu–C_2N_1$ and $Ag–C_2N_1$ monolayer is illustrated when exposed to a range of gases emitted due to battery instability. This exposure highlights their distinctive

capacity for selectively adsorbing NO_2, notably emphasized within $Cu–C_2N_1$. Both monolayers exhibit commendable hydrophobic properties. Additionally, considering the impact of temperature on the material's performance, it is essential to analyze the Gibbs free energy of the material to assess the practical temperature range for its use. The detailed calculation process can be referred to the ESI.†

The more negative the free energy, the more likely a spontaneous adsorption occurs. This study calculates Gibbs free energy at various temperatures to identify intervals where the free energy is below zero. Therefore, the actual applicable temperature range of $Ag–C_2N_1$ and $Cu–C_2N_1$ is determined. Fig. 6b and c show the linear relationship between the Gibbs free energy and temperature of the six gases adsorbed on $Cu/Ag–C_2N_1$ at different temperatures. In Fig. 6b, $\Delta G < 0$ is observed at a minimum temperature of 500 K, indicating that $Ag–C_2N_1$ cannot adsorb certain gases at temperatures higher than 500 K. Meanwhile, Fig. 6c displays $\Delta G < 0$ at a minimum temperature of 600 K. Consequently, the high-temperature resistance of $Cu–C_2N_1$ to the adsorption of the six gases surpasses that of $Ag–C_2N_1$. Therefore, the application scope of $Cu–C_2N_1$ is broader. Selective detection of NO_2 on $Cu–C_2N_1$ in high-temperature environments is superior and applicable over a wider temperature range compared to $Ag–C_2N_1$. The noteworthy aspect is the maximum applicable temperature of 500 K on $Ag–C_2N_1$ and 600 K on $Cu–C_2N_1$, which are the upper limits for H_2O adsorption. The results of DOS analysis confirmed that humidity has no impact on the selective adsorption performance. Consequently, the actual response temperature upper limit of $Ag–C_2N_1$ is 700 K (determined by $Ag–C_2N_1–PF_5$), while for $Cu–C_2N_1$, it's 800 K (determined by $Cu–C_2N_1–C_2H_6$). The $Cu–C_2N_1$ monolayer's applicable temperature surpasses the hot mixture's maximum temperature released after battery damage (470 to 720 K) and remains minimally affected by humidity, making it suitable for a wide range of environments.

For the gas diffusion performance of $Cu/Ag–C_2N_1$, molecular dynamics simulations were used to calculate the diffusion coefficient. The detailed calculation can be found in the ESI.† The diffusion coefficient plays a critical role as it quantifies the gas's diffusion capacity. A larger diffusion coefficient corresponds to a faster diffusion rate, indicating a lower energy barrier required for diffusion.[62,63] In order to explore the diffusion behavior of gases on the monolayer, the diffusion coefficients of the six gas molecules on the monolayer were calculated. The initial and the final stable configurations are shown in Fig. S21 and S22.† $Cu–C_2N_1–NO_2$ has the smallest diffusion coefficient as shown in Table S2,† which further proved that the monolayer of $Cu–C_2N_1$ can achieve selective adsorption of NO_2 gas. Interestingly, the diffusion coefficient of water is the largest, indicating that the monolayer does not attract much water.

NO_2 exhibits the lowest diffusion rate on the monolayer. To comprehend its underlying mechanism from a physicochemical perspective, NO_2 diffusion activation energy was obtained by fitting the Arrhenius equation according to the diffusion coefficient. The detailed calculation can be referred to the ESI.† The stable structures of $Cu–C_2N_1–NO_2$ at different temperatures

15260 | *J. Mater. Chem. A*, 2024, **12**, 15254–15264

This journal is © The Royal Society of Chemistry 2024
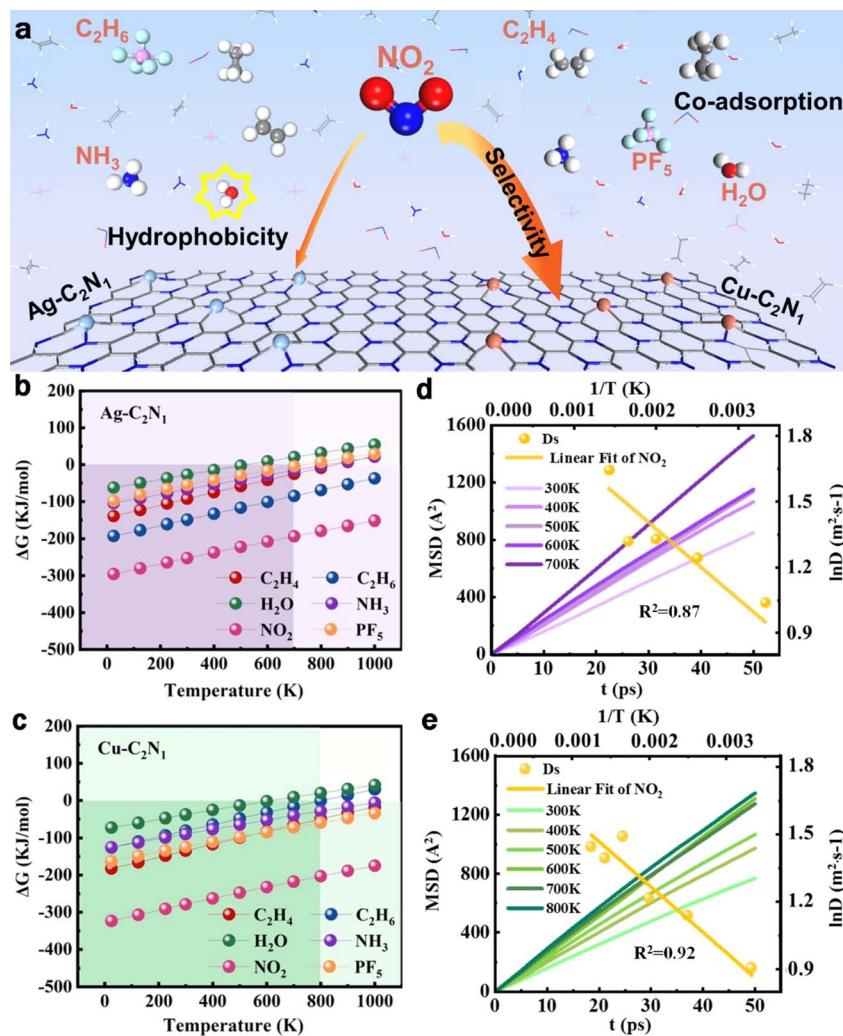
Fig. 6 (a) Schematic diagram of the high selectivity and hydrophobicity of Cu/Ag–C_2N_1. The Gibbs free energy of the six gases on (b) Ag–C_2N_1 and (c) Cu–C_2N_1 as a function of temperature. Gas diffusion and mean-squared displacement on (d) Ag–C_2N_1 and (e) Cu–C_2N_1 at different temperatures.

are shown in Fig. S23 and S24.† The level of activation energy directly affects both the difficulty and the rate of adsorption in the process.[64,65] The smaller the activation energy, the less energy is required, making the adsorption more likely to occur. As shown in Fig. 6d and e, the mean-squared displacement of NO_2 on Ag/Cu–C_2N_1 in the effective applicable temperature range shows that the diffusion activation energy of Cu–C_2N_1 (2.5 kJ mol^{-1}) is less than that of Ag–C_2N_1 (2.7 kJ mol^{-1}). Thus, it is confirmed that Cu–C_2N_1 has more advantages than Ag–C_2N_1 in the field of NO_2 detection.

In the practical sensor usage, assessing gas molecule recovery time performance is crucial. The recovery time (τ) is defined as the time taken by a sensor to return to its original state, when the gas is removed. According to transition state theory, τ is calculated as:[16]

$$\tau = \nu^{-1} \mathrm{e}^{-E_{ads}/kT} \qquad (4)$$

where ν is the attempt frequency (determined to be 10^{12} s^{-1}), k represents the Boltzmann constant, and T is the temperature.

Tables S4 and S5† detail the τ of the six gases (C_2H_4, C_2H_6, NH_3, NO_2, H_2O, and PF_5) adsorbed on the monolayers at varied temperatures. Overall, as temperatures rise, the τ decreases, indicating accelerated gas desorption. The Cu–C_2N_1 monolayer exhibits longer desorption times compared to Ag–C_2N_1, with NO_2 displaying prolonged τ due to its robust adsorption energy, aligning with experimental observations.[26] Notably, in scenarios of battery damage and high-temperature gas release, the Cu–C_2N_1 monolayer continues to exhibit high selectivity to NO_2, demonstrating its advanced nature.

3 Conclusions

In summary, the gas-sensitive behavior on Cu/Ag–C_2N_1 was clarified by dispersion-corrected DFT calculations. The results show that Cu and Ag can be anchored to the monolayer of the C_2N_1 material. After doping metal atoms, the cohesion energy was compared to illustrate the monolayer stability. By DOS analysis, Cu decorated C_2N_1 improved conductivity better than the Ag atom. Moreover, NO_2 prefers to adsorb on Cu–C_2N_1 due

This journal is © The Royal Society of Chemistry 2024

J. Mater. Chem. A, 2024, **12**, 15254–15264 | **15261**

to its obvious electronic overlap. The adsorption energy of NO_2 for Cu–C_2N_1 is −3.54 eV, and that of NO_2 for Ag–C_2N_1 is −3.27 eV. The adsorption of NO_2 by Cu–C_2N_1 is significant as also demonstrated by charge transfer, bond length and COHP. Thus, Cu–C_2N_1 has a stronger affinity for NO_2. Notably, we clearly show for the first time in the DOS analysis that Cu–C_2N_1 achieves a single electrical response to NO_2 while eliminating other gaseous disturbances. Furthermore, we also use d-band-center theory to understand the underlying mechanism of gas adsorption on the Cu/Ag–C_2N_1 monolayer. In terms of practicality, the temperature application range of the modified Cu–C_2N_1 (<800 K) is higher than that of Ag–C_2N_1 (<700 K). Interestingly, the adsorption and response of H_2O were extremely poor, demonstrating the minimal effect of humidity on the monolayer. Molecular dynamics simulations revealed that the fundamental reason for the difference in the diffusion performance of NO_2 on the monolayers is that Cu–C_2N_1 has a lower diffusion activation energy barrier (2.5 kJ mol^{-1}). When considering cost, Cu proves to be considerably more economical than Ag. Our research confirms that Cu–C_2N_1 surpasses the Ag–C_2N_1 in both adsorption and response to NO_2 gas. Thus, the Cu–C_2N_1 monolayer can be used as a gas sensor for gas generated by degassed products, greatly increasing the chances of successfully developing a new prototype of safety monitoring.

Data availability

Data will be made available on request.

Author contributions

Mingyang Gu: data curation, formal analysis, investigation, methodology, writing – original draft, and writing – review & editing. Lin Tao: validation, data curation, methodology, supervision, funding acquisition, conceptualization, validation, and writing – review & editing. Davoud Dastan: methodology, supervision, and resources. Jie Dang: methodology, formal analysis, and software. Timing Fang: methodology, formal analysis, and software. Baigang An: supervision, formal analysis, and writing – review & editing.

Conflicts of interest

The authors declare that they have no known competing financial interests or personal relationships that could have appeared to influence the work reported in this paper.

Acknowledgements

References

1 J. B. Goodenough and K. S. Park, The Li-ion rechargeable battery: a perspective, *J. Am. Chem. Soc.*, 2013, **135**, 1167–1176.

2 A. Manthiram, An Outlook on Lithium Ion Battery Technology, *ACS Cent. Sci.*, 2017, **3**, 1063–1069.

3 M. Armand and J. M. Tarascon, Building better batteries, *Nature*, 2008, **451**, 652–657.

4 A. M. Bates, Y. Preger, L. Torres-Castro, K. L. Harrison, S. J. Harris and J. Hewson, Are solid-state batteries safer than lithium-ion batteries?, *Joule*, 2022, **6**, 742–755.

5 Y. Chen, Y. Kang, Y. Zhao, L. Wang, J. Liu, Y. Li, Z. Liang, X. He, X. Li, N. Tavajohi and B. Li, A review of lithium-ion battery safety concerns: The issues, strategies, and testing standards, *J. Energy Chem.*, 2021, **59**, 83–99.

6 D. Santos-Carballal, O. Lupan, N. Magariu, N. Ababii, H. Krüger, M. T. Bodduluri, N. H. de Leeuw, S. Hansen and R. Adelung, Al_2O_3/ZnO composite-based sensors for battery safety applications: An experimental and theoretical investigation, *Nano Energy*, 2023, **109**, 108301.

7 O. Lupan, N. Magariu, D. Santos-Carballal, N. Ababii, J. Offermann, P. Pooker, S. Hansen, L. Siebert, N. H. de Leeuw and R. Adelung, Development of 2-in-1 Sensors for the Safety Assessment of Lithium-Ion Batteries via Early Detection of Vapors Produced by Electrolyte Solvents, *ACS Appl. Mater. Interfaces*, 2023, **15**, 27340–27356.

8 P. Liu, L. Yang, B. Xiao, H. Wang, L. Li, S. Ye, Y. Li, X. Ren, X. Ouyang, J. Hu, F. Pan, Q. Zhang and J. Liu, Revealing Lithium Battery Gas Generation for Safer Practical Applications, *Adv. Funct. Mater.*, 2022, **32**, 2208586.

9 H. Cui, C. Yan, P. Jia and W. Cao, Adsorption and sensing behaviors of SF_6 decomposed species on Ni-doped C_3N monolayer: A first-principles study, *Appl. Surf. Sci.*, 2020, **512**, 145759.

10 D. Chen, X. Zhang, H. Xiong, Y. Li, J. Tang, S. Xiao and D. Zhang, A First-Principles Study of the SF_6 Decomposed Products Adsorbed Over Defective WS_2 Monolayer as Promising Gas Sensing Device, *IEEE Trans. Device Mater. Reliab.*, 2019, **19**, 473–483.

11 S. Zhai, X. Jiang, D. Wu, L. Chen, Y. Su, H. Cui and F. Wu, Single Rh atom decorated pristine and S-defected PdS_2 monolayer for sensing thermal runaway gases in a lithium-ion battery: A first-principles study, *Surf. Interfaces*, 2023, **37**, 102735.

12 K. Boonpalit, J. Kinchagawat, C. Prommin, S. Nutanong and S. Namuangruk, Efficient exploration of transition-metal decorated MXene for carbon monoxide sensing using integrated active learning and density functional theory, *Phys. Chem. Chem. Phys.*, 2023, **25**, 28657–28668.

13 B. Mondal, X. Zhang, S. Kumar, F. Long, N. K. Katiyar, M. Kumar, S. Goel and K. Biswas, A resistance-driven H(2) gas sensor: high-entropy alloy nanoparticles decorated 2D MoS(2), *Nanoscale*, 2023, **15**, 17097–17104.

14 P. Li, R. Zhou, B. Liu, Y. Yuan, H. Cui, Z.-H. Pu and T. Wu, Adsorption of a $MoSe_2$-Based Sensor for Fluorocarbon Gas

Decomposition Products in Gas-Insulated Switchgear: A First Principles Analysis, *J. Phys. Chem. C*, 2023, **127**, 11176–11185.

15 H. Cui, T. Yang, X. Peng and G. Zhang, First-principles screening upon Janus PtXY (X, Y = S, Se and Te) monolayer under applied biaxial strains and electric fields, *J. Mater. Res. Technol.*, 2022, **18**, 1218–1229.

16 D. Chen, X. Zhang, J. Tang, Z. Cui and H. Cui, Pristine and Cu decorated hexagonal InN monolayer, a promising candidate to detect and scavenge SF6 decompositions based on first-principle study, *J. Hazard. Mater.*, 2019, **363**, 346–357.

17 C. Anichini, W. Czepa, D. Pakulski, A. Aliprandi, A. Ciesielski and P. Samori, Chemical sensing with 2D materials, *Chem. Soc. Rev.*, 2018, **47**, 4860–4908.

18 X. Sun, Q. Yang, R. Meng, C. Tan, Q. Liang, J. Jiang, H. Ye and X. Chen, Adsorption of gas molecules on graphene-like InN monolayer: A first-principle study, *Appl. Surf. Sci.*, 2017, **404**, 291–299.

19 L. Tao, D. Dastan, W. Wang, P. Poldorn, X. Meng, M. Wu, H. Zhao, H. Zhang, L. Li and B. An, Metal-Decorated InN Monolayer Senses N_2 against CO_2, *ACS Appl. Mater. Interfaces*, 2023, **15**, 12534–12544.

20 H. Cui, X. Zhang, Y. Li, D. Chen and Y. Zhang, First-principles insight into Ni-doped InN monolayer as a noxious gases scavenger, *Appl. Surf. Sci.*, 2019, **494**, 859–866.

21 H. Ye, S. Liu, K. Peng, Q. Zheng, J. Hu and H. Cui, Exploration of Pt-doped Janus WSSe monolayer as a typical gas sensor for condition assessment in XLPE cables, *Chem. Phys. Lett.*, 2023, **832**, 140880.

22 B. Pecz, G. Nicotra, F. Giannazzo, R. Yakimova, A. Koos and A. Kakanakova-Georgieva, Indium Nitride at the 2D Limit, *Adv. Mater.*, 2021, **33**, 2006660.

23 P. Hess, Bonding, structure, and mechanical stability of 2D materials: the predictive power of the periodic table, *Nanoscale Horiz.*, 2021, **6**, 856–892.

24 T. Zhang, L. Li, T. Huang, H. Wan, W.-Y. Chen, Z.-X. Yang, G.-F. Huang, W. Hu and W.-Q. Huang, Correlation between spin state and activity for hydrogen evolution of PtN_2 monolayer, *Appl. Phys. Lett.*, 2024, **124**, 063903.

25 W.-Y. Chen, L. Li, T. Huang, Z.-X. Yang, T. Zhang, G.-F. Huang, W. Hu and W.-Q. Huang, Extending Schottky–Mott rule to van der Waals heterostructures of 2D Janus materials: Influence of intrinsic dipoles, *Appl. Phys. Lett.*, 2023, **123**, 171601.

26 Y. Liu, L. Gao, S. Fu, S. Cheng, N. Gao and H. Li, Highly efficient VOC gas sensors based on Li-doped diamane, *Appl. Surf. Sci.*, 2023, **611**, 155694.

27 X. Tang, G. Guo, Y. Peng, M. You, S. Luo, C. He, C. Tang, Z. Huang and J. Zhong, Tunable properties of two-dimensional bilayer C_3N as anode material: Bandgap, binding energy, and diffusion barrier, *J. Energy Storage*, 2024, **77**, 109906.

28 X. Wang, H. Niu, X. Wan, A. Wang, F. R. Wang and Y. Guo, Impact of Coordination Environment on Single-Atom-Embedded C_3N for Oxygen Electrocatalysis, *ACS Sustain. Chem. Eng.*, 2022, **10**, 7692–7701.

29 Z. Chen, J. Zhao, C. R. Cabrera and Z. Chen, Computational Screening of Efficient Single-Atom Catalysts Based on Graphitic Carbon Nitride (g-C_3N_4) for Nitrogen Electroreduction, *Small Methods*, 2018, **3**, 1800368.

30 P. Kaur, S. Bagchi, D. Gribble, V. G. Pol and A. P. Bhondekar, Impedimetric Chemosensing of Volatile Organic Compounds Released from Li-Ion Batteries, *ACS Sens.*, 2022, **7**, 674–683.

31 P. Kaur, S. Bagchi, V. G. Pol and A. P. Bhondekar, Early Detection of Mixed Volatile Organic Compounds to Circumvent Calamitous Li-Ion Battery Thermal Runaway, *J. Phys. Chem. C*, 2023, **127**, 8373–8382.

32 M. Wu, S. Han, S. Liu, J. Zhao and W. Xie, Fire-safe polymer electrolyte strategies for lithium batteries, *Energy Storage Mater.*, 2024, **66**, 103174.

33 H. Xiong, H. Zhang and L. Gan, A new bifunctional C_3N nanosheet of NO_2, SO_2 gas sensor and CO_2 separation: A first-principles study, *Phys. E*, 2021, **126**, 114463.

34 H. Cui, G. Zhang, X. Zhang and J. Tang, Rh-doped $MoSe_2$ as a toxic gas scavenger: a first-principles study, *Nanoscale Adv.*, 2019, **1**, 772–780.

35 L. Li, H. Cao, Z. Liang, Y. Cheng, T. Yin, Z. Liu, S. Yan, S. Jia, L. Li, J. Wang and Y. Gao, First-Principles Study of Ti-Deficient Ti_3C_2 MXene Nanosheets as NH_3 Gas Sensors, *ACS Appl. Nano Mater.*, 2022, **5**, 2470–2475.

36 D. Dastan, K. shan, A. Jafari, T. Marszalek, M. K. A. Mohammed, L. Tao, Z. Shi, Y. Chen, X.-T. Yin, N. D. Alharbi, F. Gity, S. Asgary, M. Hatamvand and L. Ansari, Influence of heat treatment on H_2S gas sensing features of NiO thin films deposited *via* thermal evaporation technique, *Mater. Sci. Semicond. Process.*, 2023, **154**, 107232.

37 P. Lv, D. Wu, B. He, X. Li, R. Zhu, G. Tang, Z. Lu, D. Ma and Y. Jia, An efficient screening strategy towards multifunctional catalysts for the simultaneous electroreduction of NO_3-, NO_2- and NO to NH_3, *J. Mater. Chem. A*, 2022, **10**, 9707–9716.

38 M. Tang, D. Zhang, D. Wang, J. Deng, D. Kong and H. Zhang, Performance prediction of 2D vertically stacked MoS_2-WS_2 heterostructures base on first-principles theory and Pearson correlation coefficient, *Appl. Surf. Sci.*, 2022, **596**, 153498.

39 D. Chen, Y. Li, S. Xiao, C. Yang, J. Zhou and B. Xiao, Single Ni atom doped WS_2 monolayer as sensing substrate for dissolved gases in transformer oil: A first-principles study, *Appl. Surf. Sci.*, 2022, **579**, 152141.

40 L. T. Ta, I. Hamada, Y. Morikawa and V. A. Dinh, Adsorption of toxic gases on borophene: surface deformation links to chemisorptions, *RSC Adv.*, 2021, **11**, 18279–18287.

41 W. Nong, H. Liang, S. Qin, Y. Li and C. Wang, Computational Design of Two-Dimensional Boron-Containing Compounds as Efficient Metal-free Electrocatalysts toward Nitrogen Reduction Independent of Heteroatom Doping, *ACS Appl. Mater. Interfaces*, 2020, **12**, 50505–50515.

This journal is © The Royal Society of Chemistry 2024

J. Mater. Chem. A, 2024, **12**, 15254–15264 | **15263**

42 M. I. Ahmed, L. J. Arachchige, Z. Su, D. B. Hibbert, C. Sun and C. Zhao, Nitrogenase-Inspired Atomically Dispersed Fe–S–C Linkages for Improved Electrochemical Reduction of Dinitrogen to Ammonia, *ACS Catal.*, 2022, **12**, 1443–1451.

43 Q. Yue, Z. Shao, S. Chang and J. Li, Adsorption of gas molecules on monolayer MoS_2 and effect of applied electric field, *Nanoscale Res. Lett.*, 2013, **8**, 425.

44 H. Wang, X. Li, J. Wu and D. Zhang, An Experimental and Density Functional Theory Simulation Study of NO Reduction Mechanisms over Fe(0) Supported on Graphene with and without CO, *Langmuir*, 2023, **39**, 15369–15379.

45 L. Tao, J. Huang, D. Dastan, T. Wang, J. Li, X. Yin and Q. Wang, CO_2 capture and separation on charge-modulated calcite, *Appl. Surf. Sci.*, 2020, **530**, 147265.

46 I. S. Amiinu, X. Liu, Z. Pu, W. Li, Q. Li, J. Zhang, H. Tang, H. Zhang and S. Mu, From 3D ZIF Nanocrystals to Co-N_x/C Nanorod Array Electrocatalysts for ORR, OER, and Zn-Air Batteries, *Adv. Funct. Mater.*, 2018, **28**, 1704638.

47 M. Wang, W. Ma, C. Tan, Z. Qiu, L. Hu, X. Lv, Q. Li and J. Dang, Designing Efficient Non-Precious Metal Electrocatalysts for High-Performance Hydrogen Production: A Comprehensive Evaluation Strategy, *Small*, 2023, e2306631.

48 Z. Lv, W. Ma, M. Wang, J. Dang, K. Jian, D. Liu and D. Huang, Co-Constructing Interfaces of Multiheterostructure on MXene ($Ti_3C_2T_x$)-Modified 3D Self-Supporting Electrode for Ultraefficient Electrocatalytic HER in Alkaline Media, *Adv. Funct. Mater.*, 2021, **31**, 2102576.

49 K. He, W. Li, L. Tang, L. Chen, G. Wang, Q. Liu, X. Xin, C. Yang, Z. Wang, S. Lv and D. Xing, Insight into the design of a Ti_3C_2 MXene/Ti_4O_7 composite ceramic membrane boosts the electrocatalytic activity for 1,4-dioxane electro-oxidation, *Appl. Catal., B*, 2023, **338**, 123077.

50 S. Nie, L. Tao, J. Li, W. Wang, P. Poldorn, Y. He, X. Yin and M. Wu, A single response to reducing gases by NiO-TiO_2 heterojunction nanocrystals, *Appl. Surf. Sci.*, 2024, **644**, 158821.

51 S. Nie, J. Li, L. Tao, Y. He, D. Dastan, X. Meng, P. Poldorn and X. Yin, Insights into Selective Mechanism of NiO-TiO(2) Heterojunction to H(2) and CO, *ACS Sens.*, 2023, **8**, 4121–4131.

52 L. Tao, J. Huang, D. Dastan, T. Wang, J. Li, X. Yin and Q. Wang, New insight into absorption characteristics of CO_2 on the surface of calcite, dolomite, and magnesite, *Appl. Surf. Sci.*, 2021, **540**, 148320.

53 Y. He, L. Tao, J. Li, M. Wu, P. Poldorn, D. Dastan, S. Abbasi, S. Nie, X. Yin and Q. Wang, Atomic-level insights into selective adsorption of H_2 and CO on SnO_2/CoO heterojunctions, *Mater. Today Nano*, 2023, **22**, 100334.

54 Y. He, J. Li, L. Tao, S. Nie, T. Fang, X. Yin and Q. Wang, First-principles calculations on the resistance and electronic properties of H_2 adsorption on a CoO-SnO_2 heterojunction surface, *Phys. Chem. Chem. Phys.*, 2021, **24**, 392–402.

55 M. Wang, L. Kong, X. Lu and C.-M. Lawrence Wu, First-row transition metal embedded pyrazine-based graphynes as high-performance single atom catalysts for the CO_2 reduction reaction, *J. Mater. Chem. A*, 2022, **10**, 9048–9058.

56 J. Li, C. Hou, C. Chen, W. Ma, Q. Li, L. Hu, X. Lv and J. Dang, Collaborative Interface Optimization Strategy Guided Ultrafine RuCo and MXene Heterostructure Electrocatalysts for Efficient Overall Water Splitting, *ACS Nano*, 2023, **17**, 10947–10957.

57 L. Tao, Z. Li, G.-C. Wang, B.-Y. Cui, X.-T. Yin and Q. Wang, Evolution of calcite surface reconstruction and interface adsorption of calcite-CO_2 with temperature, *Mater. Res. Express*, 2018, **6**, 025035.

58 H. Zhang, R. Zhang, Y. Ni, M. Chen, C. Sun and F. Dong, SO_2 adsorption and conversion on pristine and defected calcite {1 0 4} surface: A density functional theory study, *Appl. Surf. Sci.*, 2022, **596**, 153575.

59 L. Lin, S. Yao, R. Gao, X. Liang, Q. Yu, Y. Deng, J. Liu, M. Peng, Z. Jiang, S. Li, Y. W. Li, X. D. Wen, W. Zhou and D. Ma, A highly CO-tolerant atomically dispersed Pt catalyst for chemoselective hydrogenation, *Nat. Nanotechnol.*, 2019, **14**, 354–361.

60 X. Liu, Y. Jiao, Y. Zheng, M. Jaroniec and S.-Z. Qiao, Building Up a Picture of the Electrocatalytic Nitrogen Reduction Activity of Transition Metal Single-Atom Catalysts, *J. Am. Chem. Soc.*, 2019, **141**, 9664–9672.

61 H. Hu, P. Zhang, B.-B. Xiao and J.-L. Mi, Theoretical study of p-block metal–nitrogen–carbon single-atom catalysts for the oxygen reduction reaction, *Catal. Sci. Technol.*, 2022, **12**, 6751–6760.

62 L. Tao, J. Huang, X. Yin, Q. Wang, Z. Li, G. Wang and B. Cui, Adsorption Kinetics of CO_2 on a Reconstructed Calcite Surface: An Experiment-Simulation Collaborative Method, *Energy Fuels*, 2019, **33**, 8946–8953.

63 L. Tao, J. Huang, D. Dastan, J. Li, X. Yin and Q. Wang, Flue gas separation at organic-inorganic interface under geological conditions, *Surf. Interfaces*, 2021, **27**, 101462.

64 T. Fang, C. Wei, X. Meng, G. Zhou and X. Liu, How homogeneous and biphasic membranes contribute to the gas transfer: A molecular dynamics simulation study, *Int. J. Heat Mass Transfer*, 2023, **201**, 123644.

65 X. Meng, T. Fang, G. Zhou, S. Liu and X. Liu, Selectivity and permeability of gas separation in SILMs: Effect of collapsed structure, *J. Mol. Liq.*, 2023, **388**, 122834.

15264 | *J. Mater. Chem. A*, 2024, **12**, 15254–15264

This journal is © The Royal Society of Chemistry 2024